Dispersively Detected Pauli Spin-Blockade in a Silicon Nanowire Field-Effect Transistor

A. C. Betz,*,† R. Wacquez,‡ M. Vinet,‡ X. Jehl,§ A. L. Saraiva,∥ M. Sanquer,§ A. J. Ferguson,⊥ and M. F. Gonzalez-Zalba†

†Hitachi Cambridge Laboratory, J. J. Thomson Avenue, Cambridge CB3 0HE, United Kingdom
‡CEA/LETI-MINATEC, CEA-Grenoble, 17 rue des Martyrs, F-38054 Grenoble, France
§SPSMS, UMR-E CEA/UJF-Grenoble 1, INAC, 17 rue des Martyrs, 38054 Grenoble, France
∥Instituto de Fisica, Universidade Federal do Rio de Janeiro, Caixa Postal 68528, 21941-972 Rio de Janeiro, Brazil
⊥Cavendish Laboratory, University of Cambridge, Cambridge CB3 0HE, United Kingdom

Ⓢ Supporting Information

ABSTRACT: We report the dispersive readout of the spin state of a double quantum dot formed at the corner states of a silicon nanowire field-effect transistor. Two face-to-face top-gate electrodes allow us to independently tune the charge occupation of the quantum dot system down to the few-electron limit. We measure the charge stability of the double quantum dot in DC transport as well as dispersively via in situ gate-based radio frequency reflectometry, where one top-gate electrode is connected to a resonator. The latter removes the need for external charge sensors in quantum computing architectures and provides a compact way to readout the dispersive shift caused by changes in the quantum capacitance during inter-dot charge transitions. Here, we observe Pauli spin-blockade in the high-frequency response of the circuit at finite magnetic fields between singlet and triplet states. The blockade is lifted at higher magnetic fields when intra-dot triplet states become the ground state configuration. A line shape analysis of the dispersive phase shift reveals furthermore an intra-dot valley-orbit splitting Δ_{vo} of 145 μeV. Our results open up the possibility to operate compact complementary metal-oxide semiconductor (CMOS) technology as a singlet−triplet qubit and make split-gate silicon nanowire architectures an ideal candidate for the study of spin dynamics.

KEYWORDS: Double quantum dot, Pauli spin-blockade, silicon, dispersive radio frequency readout
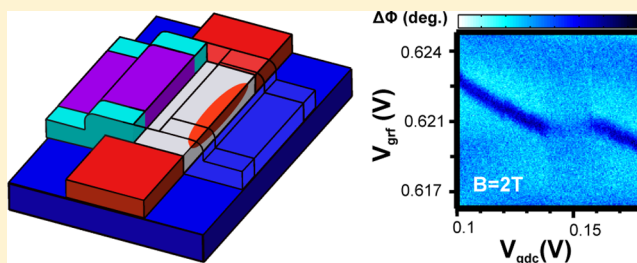
Since its first observation in electrical transport through a GaAs double quantum dot spin-blockade, or Pauli blockade, has been important for understanding and controlling the behavior of artificial atoms.[1] Spin-blockade has enabled the effect of the nuclear spin environment to be probed, showing that nuclear spins are responsible for mixing between the electron spin states.[2,3] Perhaps its biggest contribution is allowing readout of the spin state of a double quantum dot in the singlet−triplet basis.[4,5] In such experiments a charge sensor will typically monitor the response of the double quantum dot charge to an external voltage pulse, yielding an averaged or single shot measurement of the spin state.[4,6] Spin-blockade has proved to be a generic tool for quantum dots made in materials other than GaAs, and most recently is of interest in silicon[7−11] or silicon germanium,[12−14] where a reduced nuclear spin environment leads to longer spin coherence times.[15] In addition it is possible to measure spin-blockade without a charge sensor and without direct electrical transport, by performing high-frequency capacitance measurements on the double quantum dot.[16,17] Removing the need for an external charge sensor makes such quantum capacitance or dispersive

measurements attractive as it reduces the complexity of the gate architecture of the quantum dots. It also enables a double quantum dot to be interfaced with superconducting resonators,[18] a promising element for long-distance transfer of quantum information.

In this Letter, we demonstrate the in situ dispersive measurement of spin-blockade in the corner states of a double-gated silicon nanowire FET[19,20] (SiNWFET) and describe the magnetic field dependence of the high-frequency response of the system. A double quantum dot (DQD) arises as a result of electrostatics in the square channel transistor geometry.[19,21] Each dot can be tuned independently by a separate top-gate electrode, one of which is connected to a resonant circuit and provides the dispersive MHz reflectometry readout. We confirm the presence of one quantum dot per corner state and observe the double quantum dot's few-electron limit and inter-dot charge transitions. The latter manifest as an
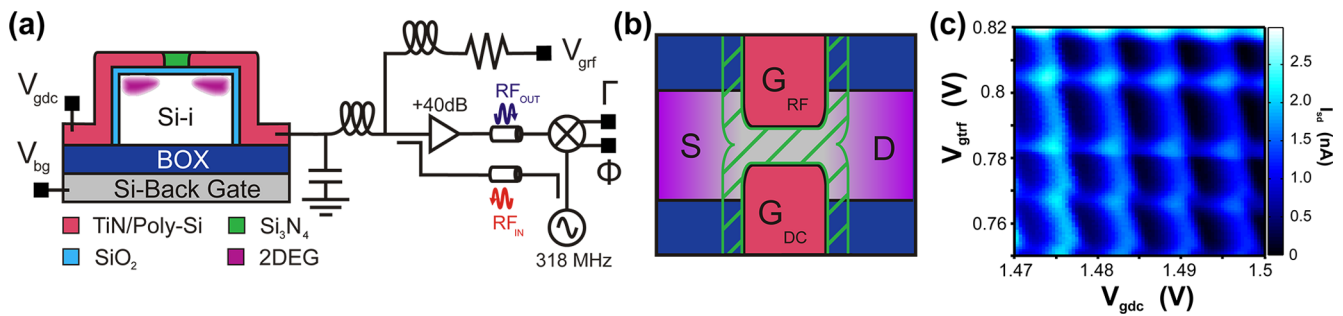
Figure 1. Device geometry and measurement setup. (a) Sketch of device cross-section perpendicular to transport direction and reflectometry setup. When the top-gates are biased just below threshold a double quantum dot is formed at the topmost corners. Gate G_{RF} is connected to resonant circuitry including a bias-tee and used to probe the high-frequency admittance of the DQD. (b) Top view sketch presenting the face-to-face top-gate design. Si_3N_4 spacers (hatched green) provide the doping gradient from the doped source/drain to the intrinsic channel and separate the top-gates G_{DC} and G_{RF}. (c) DC charge stability diagram of the double quantum dot in the multielectron regime at V_{sd} = 3 mV and V_{bg} = −0.5 V. The honeycomb pattern, typical for interacting quantum dots, indicates low cross-coupling capacitance.
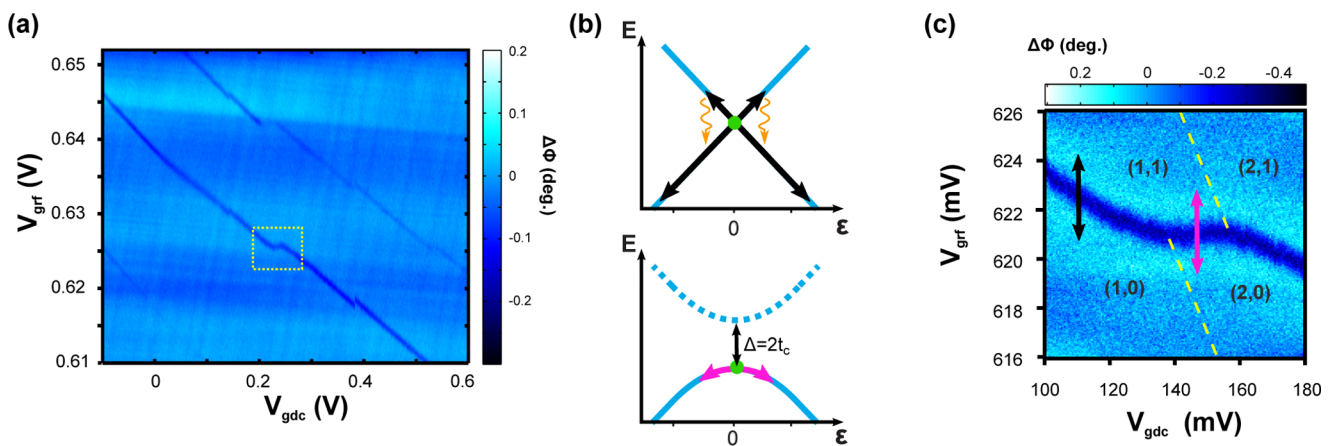
Figure 2. Dispersive gate based RF readout in the few electron regime. (a) Stability diagram at V_{sd} = 0 V and V_{bg} = −1 V. Only lines originating from QD_{RF} are detected by the gate sensor. The dashed square indicates the transition shown in panel c. (b) RF readout model. Top: For lead-dot transitions the system is modeled by two crossing levels. The signal arises from a charge being cyclically driven across the charge instability at V_0 by the RF excitation ΔV_g (black arrows) and the subsequent relaxation (orange). Bottom: inter-dot transitions are measurable due to the additional quantum capacitance that arises from the band curvature at the anticrossing. ϵ is the inter-dot detuning. (c) Close-up of inter-dot transition. The arrows indicate the two measurement modes shown in panel b. The dashed lines are an approximation of the lines of QD_{DC}.

additional capacitance contribution, readily captured by the dispersive gate sensor. We use this to selectively readout the spin state of a singlet−triplet charge transition under finite magnetic field. Furthermore, we observe lifting of the blockade at higher magnetic fields due to anticrossing triplet states. Our work shows a compact way to measure spin-blockade in a device processed using standard industrial fabrication, paving the way toward fully complementary metal-oxide semi-conductor (CMOS)-compatible quantum computing architectures.[22]

The device presented here is a fully depleted silicon-on-insulator (SOI) nanowire transistor.[23,24] Figure 1a shows a cross-section of the transistor perpendicular to the transport direction. It consists of an undoped Si (001) channel of thickness t_{Si} = 12 nm and width W = 100 nm on top of a 150 nm SiO_2 buried oxide (BOX). The underlying Si wafer serves as global back-gate. The channel is furthermore locally controlled by two face-to-face top-gate electrodes (length L = 60 nm), separated from the channel by 5 nm of SiO_2 (Figure 1a,b) and at a distance of 70 nm from each other. The electrical isolation between them is provided by Si_3N_4 spacers, which extend 40 nm toward source and drain to prevent dopant diffusion from the highly doped contacts into the channel

during fabrication (see Figure 1b). Measurements are taken via DC transport, recording the source-drain current I_{sd}, and via gate-based reflectometry readout,[21,25] both carried out at the base temperature of a dilution refrigerator. A schematic of the reflectometry setup is shown in Figure 1a: Gate electrode G_{RF} is coupled to a resonant LC circuit that consists of a surface mount inductor (L = 390 nH) and the device's parasitic capacitance to ground ($C_p \simeq$ 500 fF). The DC voltage V_{grf} across G_{RF} is provided via an on-board bias-tee. We apply an RF tone of power −88 dBm at the tank circuit's resonant frequency ($f_r = 1/(2\pi(LC_p)^{1/2}) \simeq$ 318 MHz). Here, magnitude Γ and phase Φ of the reflected signal are sensitive to changes in the device admittance and ultimately arise from excess power dissipation and susceptance changes, respectively.[21,25−27] In particular, the phase response $\Delta\Phi$ relates to an effective change in capacitance of the system, ΔC, given by $\Delta\Phi \approx -\pi Q \Delta C / C_p$.[27] Here, Q is the quality factor of the resonator. We obtain Γ and Φ from IQ-demodulation, after the signal has been amplified at low and room temperature.

As displayed in Figure 1a, the channel has a square cross-section and the top-gates cover two channel sides (or parts thereof) each. The electric field exerted by the gate electrodes is strongest at the topmost corner of the channel, where two gate

faces meet. Charge accumulation in SiNWFETs occurs therefore first under the topmost corners, due to this so-called corner effect.[28] The corner states are furthermore confined in SD-direction by the large spacers, resulting in a quantum dot under each corner[19,21] and tunnel coupled to source and drain as well as to the other dot. We confirm the formation of the aforementioned double quantum dot in the DC transport measurement of Figure 1c. It shows the source-drain current I_{sd} as a function of both DC top-gate voltages V_{gdc} and V_{grf} in the multielectron regime at V_{sd} = 3 mV and V_{bg} = −0.5 V. We observe the honeycomb diagram characteristic for coupled double quantum dots. The DQD is in parallel configuration, which allows us to observe transport not only at the triple points, as it is commonly seen in serial DQDs,[29] but also the individual transport lines of each dot. Conduction is however increased at the triple points, due to the increase in charge transport pathways. From the honeycomb diagram, we extract the gate voltage spacing $\Delta V_{gdc(grf)}$ = 7(17) mV. Moreover, V_{sd}–V_{gxx} maps of the individual dots, obtained with the respective other dot biased largely below threshold, indicate charging energies E_C = 3−5 meV and lever arms $\alpha = C_g/C_\Sigma \simeq 0.29$ (G_{RF}) and 0.45 (G_{DC}) where C_Σ is the total and C_g the gate capacitance of the respective dot (see Supporting Information). We note that the individual transport lines in Figure 1c only vary little with respect to the opposite gate voltage, which indicates low cross-coupling capacitances C_c = 1.4−2.0 aF. Finally, from the shift produced in the vertical and horizontal lines due to the charging of an electron in the opposite dot we infer a mutual capacitance C_m = 5 aF. The main feature here, from a quantum information processing point of view, is the possibility to individually and independently control two coupled quantum dots fabricated in an industry-standard CMOS transistor.

We turn now to the high-frequency response of the system. Figure 2a shows the dispersive measurement of the DQD's charge stability in the few-electron regime, obtained via gate-based RF detection where we plot the change in phase $\Delta\Phi$. Only electron transitions involving the dot QD_{RF} under gate G_{RF} are visible now (dark blue diagonal traces) since the resonant circuit is coupled strongly to QD_{RF} via G_{RF} and only weakly to the other dot QD_{DC}. The signal corresponds to cyclic single-charge tunnelling between the source or drain and QD_{RF} driven by the MHz tone applied to the resonator. In this case, the system can be modeled as inelastic charge transitions in a fast-driven two-level system,[21,26] as shown in the top panel of Figure 2b. Electrons tunnelling out-of-phase with the RF-drive lead to an additional tunnelling capacitance contribution, which manifests as a phase change in the resonator's response. Besides simplifying the architecture, the advantage of this charge readout technique is that no direct transport is necessary, only the possibility to cyclically exchange electrons between a reservoir and the probed quantum dot. As in the multielectron regime of Figure 1c, we find very little cross-coupling between the gates (note the difference in x and y scales) and a similar voltage spacing ΔV_{grf}. The kinks observable in QD_{RF}'s transition lines indicate coupling to charge transitions separate from QD_{RF}. We attribute this to QD_{DC}, which in this low voltage regime seems to be disordered due to surface roughness:[19] The voltage spacing ΔV_{gdc} has increased from the multielectron regime and has become more irregular.

Figure 2c shows a zoom into the region of one of the first transitions into QD_{DC}. The line corresponding to the loading of an electron into QD_{RF} (black arrow) is interjected by a ridge

corresponding to inter-dot charge exchange. Yellow dashed lines furthermore approximate the position of lead-QD_{DC} transitions. We attribute the presence of signal along the inter-dot ridge to a mechanism different to tunnelling capacitance described previously: Tunnel coupling t between QD_{RF} and QD_{DC} causes the DQD energy bands to hybridize with energies $E_\pm = \pm(\epsilon^2 + (2t)^2)^{1/2}/2$, as displayed in the lower panel of Figure 2b as a function of detuning ϵ. For $f_r < t/h$, there is no tunnelling capacitance since the charge remains in the ground state, while the RF drive cycles it across the inter-dot line. However, an additional capacitance contribution now arises from the band curvature, the so-called quantum capacitance[30,31]

$$C_q^\pm = -(e\alpha)^2 \frac{\partial^2 E_\pm}{\partial \epsilon^2} \tag{1}$$

where e is the charge of the electron and α the resonator-DQD coupling given by the gate lever arm.[16] C_q's capacitance contribution is maximum at $\epsilon = 0$ and positive (negative) for the ground (excited) state. The capacitance change due to C_q is picked up dispersively by the gate sensor (magenta arrow in Figure 2c). This renders the inter-dot transition visible and makes it possible to not only probe the interaction of QD_{RF} with a charge reservoir via tunneling capacitance, but also the hybridized double quantum dot with the compact dispersive gate-sensor. Note that we estimated electron occupation numbers in the form (QD_{DC}, QD_{RF}) in Figure 2c. The absence of further transition kinks toward lower V_{gdc} in Figure 2a indicates that we likely observe the first electrons into QD_{DC}. For QD_{RF}, although we have labeled the inter-dot transition (1,1)−(2,0) as a guide, the electron number corresponds to the valence occupancy. However, it becomes clear below that this transition is also among the last few electrons of QD_{RF}.

We now turn to the investigation of spin-related effects in the DQD and in particular in the inter-dot transition of Figure 2c. In the following, we demonstrate that Figure 2c depicts an even parity, spin-dependent transition. The reason for this becomes clear when we apply a magnetic field: Figure 3b shows the inter-dot transition in question at B = 2 T. We find that while the tunnelling capacitance signal of the lead-dot transitions remains unchanged, the inter-dot ridge vanishes with increasing magnetic field, as can be seen in Figure 3c. Here, we show traces across the inter-dot ridge at V_{gdc} = 0.15 V for different magnetic fields. We attribute loss of inter-dot signal to Pauli spin-blockade between a joint singlet $S(2,0)$ and a separated triplet $T(1,1)$ (Figure 3a), as predicted theoretically[32] and observed experimentally, e.g., in InAs DQDs[17] with similar phase shifts. At zero magnetic field, the ground state of the system at zero detuning is singlet, and the resonator is sensitive to its finite quantum capacitance as depicted in Figure 2c. For $B \neq 0$, however, the triplet state is Zeeman-split into T_0 and $T_\pm$, with the latter spaced at $\Delta E = \pm g\mu_B B$ from T_0.[33] Here, g is the electron spin g-factor and μ_B the Bohr magneton. When $g\mu_B B > t$, the $T_-(1,1)$ state becomes the ground state at zero detuning. As a result inter-dot phase signal decreases since $T_-(1,1)$ is linear in ϵ, i.e., has no capacitive contribution due to its lack of band curvature (see eq 1), as observed in Figure 3c. We furthermore analyze the B = 0 T trace quantitatively by fitting it with the equation

$$\Delta\Phi \propto e^2 \frac{(2t)^2}{[\alpha^2(V_{grf} - V_{grf}^0)^2 + (2t)^2]^{(3/2)}} \tag{2}$$
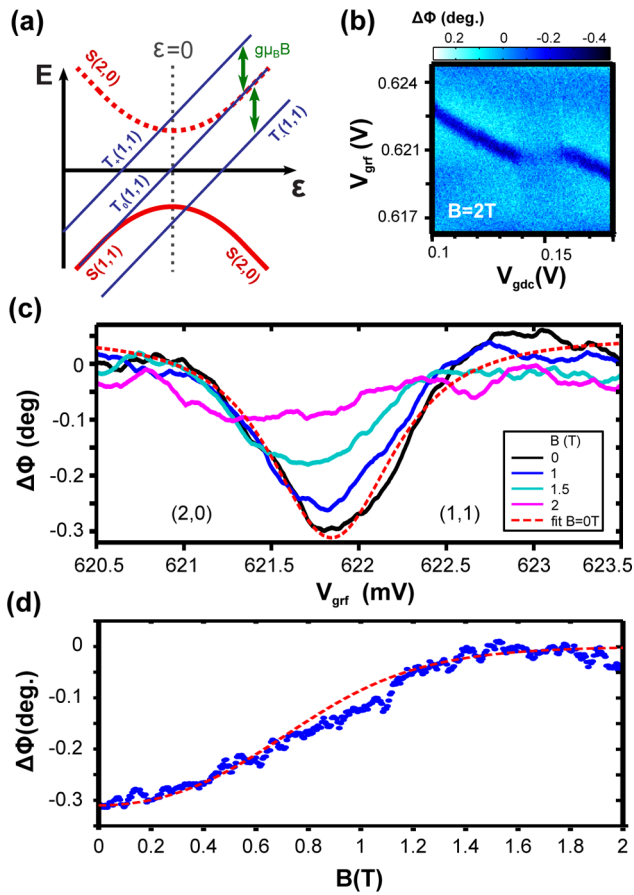
Figure 3. Dispersive spin-blockade readout. (a) Schematic of the energy bands in the DQD, including singlet and triplet lines. The triplet configuration separates into T_+, T_0, and T_- spaced at $\Delta E = g\mu_B B$. (b) Close-up of inter-dot transition of Figure 2c for finite magnetic field. Transitions into T_- at $\epsilon < 0$ reduce the inter-dot phase signal. (c) Traces $\Delta\Phi(V_{grf})$ for different magnetic fields taken at $V_{gdc} = 0.15$ V. The quantum capacitance signal decreases with increasing magnetic field due to the aforementioned transitions. (d) Phase signal at the inter-dot transition as a function of magnetic field (blue circles) and fit according to eq 4 (red line) with $t_s = 80\ \mu$eV.

obtained from eq 1, the hybridized DQD energy branches, and $\Delta\Phi \propto \Delta C$. The result is indicated by the dashed line in Figure 3c. Owing to the low cross-capacitance we use the lever arm $\alpha \simeq 0.3$ found previously for the conversion between gate voltage and detuning energy,[29] and find a tunnel coupling $t \simeq 80\ \mu$eV for the transition studied here. The magnetic field dependence of the dispersive signal at this transition is explored in Figure 3d: As expected from the reasoning above, the signal is maximum at $B = 0$ T. Due to Pauli spin blockade the dispersive shift then decreases with magnetic field until $\Delta\Phi = 0$. By adapting the analysis of ref 17, we fit the magnetic field dependence to a Boltzmann distributed probability of being in the lower singlet branch S_g (positive C_q) and subtract the probability of being in the upper singlet branch S_e (negative C_q) at zero detuning: $A \times (P_{sg} - P_{se})$. A is a scaling factor. S_g and S_e contribute with opposite sign, whereas triplet states T_0 and $T_\pm$ do not contribute to the dispersive signal.[17] The energy difference with respect to S_g for the manifold of microstates used in the fit is given by

$$\Delta E(S_g) = 0 \quad \Delta E(S_e) = 2t_s$$
$$\Delta E(T_0) = t_s \quad \Delta E(T_\pm) = t_s \pm g\mu_B B \quad (3)$$

and data fit by the thermal average

$$\langle P_{Sg} - P_{Se} \rangle = \frac{1 - e^{-2t_s/k_B T_e}}{Z(T_e, t_s)} \quad (4)$$

Here $Z(T_e, t_s) = \sum_{X_i} e^{-\Delta E(X_i)/k_B T_e}$ is the partition function of the five microstates X_i under consideration, k_B the Boltzmann constant, t_s the singlet tunnel coupling, and T_e the electron temperature. The result is shown in red in Figure 3d. Using $t_s = 80\ \mu$eV from the line shape analysis and T_e as free parameter, we obtain an electron temperature $T_e \simeq 350$ mK. In total, the above results demonstrate that it is possible to readout the spin state of individual electrons in our SiNWFET geometry, one of the essential ingredients to implement an interacting spin qubit in standard CMOS technology.

Finally, we explore spin-blockade lifting via triplet tunnelling. The band diagram discussed above only takes into account separated triplets, as $T(2,0)$ states are generally elevated in energy due to intra-dot valley-orbit coupling in silicon.[34−36] The $T(1,1)$ and $T(2,0)$ states hybridize similarly to the singlet branch, and a second anticrossing develops as sketched on the left of Figure 4a for zero magnetic field. This anticrossing appears at $\epsilon \neq 0$ when the singlet and triplet branches are separated by the valley-orbit splitting Δ_{vo}. The tunnel couplings are given by t_s and t_t for singlet and triplet anticrossing, respectively. Analogous to the $T(1,1)$ states, the $(2,0)$ triplets Zeeman-split into $T_0(2,0)$, $T_+(2,0)$, and $T_-(2,0)$ and the T_- branch becomes the DQD's ground state when $g\mu_B B > \Delta_{vo}$. For simplicity we only show the singlet and T_- branch in Figure 4a.

We have investigated this scenario in the measurement shown in Figure 4b, where we perform a magnetic field sweep across an even-parity transition lying further below in voltage V_{grf} than the one studied in Figures 2c and 3. At low magnetic fields we observe in Figure 4b the decrease in dispersive signal at $V_{grf} \simeq 482.7$ mV, i.e., $\epsilon = 0$, due to a transition from singlet to triplet. With increasing field, however, a second dispersive signal arises, shifted upward in V_{grf}, i.e., positive detuning. This represents the emerging of the triplet anticrossing: Due to their newly acquired band curvature the T_- states are now detectable by the dispersive gate sensor and can be distinguished from the singlet branch due to the detuning shift. Further to the qualitative understanding presented so far, we now analyze the singlet−triplet data quantitatively. To this end, we plot in Figure 4c traces $\Delta\Phi(V_{grf})$ for $B = 0$ and 2 T, which correspond to the two scenarios of Figure 4a. At $B = 0$ T, the ground state is predominantly singlet, whereas at $B = 2$ T the triplet dominates. Fitting with eq 2, we find a singlet (triplet) tunnel coupling $t_{s(t)} \simeq 55(40)\ \mu$eV assuming, as previously, a lever arm $\alpha = 0.29$. In order to fit the triplet data, we shift the detuning to $\epsilon_t = \epsilon - \Delta_{vo}$, which furthermore allows us to infer the valley-orbit (VO) splitting Δ_{vo} from the voltage difference ΔV_{vo} between singlet and triplet lineshapes. Converting to energy via the lever arm, we obtain thus $\Delta_{vo} = 145\ \mu$eV. We confirm that the slanted nature of the corner dots, which face the (001), (010) crystal directions, does not have a significant impact on the VO splitting since our results agree well with theoretical predictions for the valley splitting (0.1−0.3 meV)[37] and previously measured values in Si (0.1 meV)[34,38] and SiGe QDs (0.12−0.27 meV).[39]
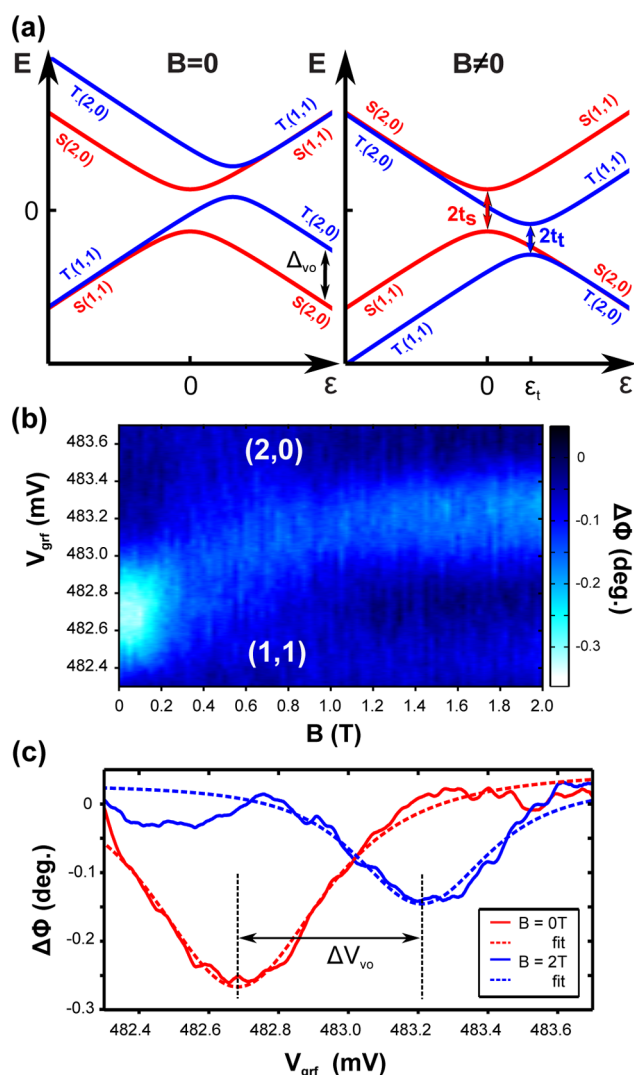
Figure 4. Spin-blockade lifting and triplet detection. (a) Schematic of lowest singlet and triplet branches at zero and finite magnetic field. (b) Phase signal as a function of V_{grf} and magnetic field. (c) Phase as a function of V_{grf} for singlet (red) and triplet (blue). Dashed lines are fits to the data following eq 2.

In conclusion, we have reported the dispersive readout of the spin state of a silicon nanowire corner state double quantum dot making use of the Pauli spin-blockade. By using a fully based CMOS device consisting of two face-to-face top gates we have achieved independent control over the two quantum dots at the corner states of a Si nanowire transistor, and by means of dispersive gate readout, we have observed the double quantum dot's few electron regime. Spin-blockade manifests as a decrease in dispersive signal in a few-electron inter-dot transition of even parity. We have furthermore presented a scenario where singlet and triplet branches can be discerned by means of magnetic field studies. Our results demonstrate that compact CMOS-based architectures are suitable to implement spin qubits. Ultimately, this fully industrial approach opens a window to larger-scale qubit architectures.

ASSOCIATED CONTENT

Ⓢ Supporting Information

Additional DC transport measurements of the coupled double-dot system performed in the multielectron regime. The

Supporting Information is available free of charge on the ACS Publications website at DOI: 10.1021/acs.nanolett.5b01306.

AUTHOR INFORMATION

Corresponding Author

*E-mail: ab2106@cam.ac.uk.

Notes

The authors declare no competing financial interest.

REFERENCES

(1) Ono, K.; Austing, D. G.; Tokura, Y.; Tarucha, S. *Science* **2002**, *297*, 1313−1317.

(2) Koppens, F. H. L.; Folk, J. A.; Elzerman, J. M.; Hanson, R.; van Beveren, L. H. W.; Vink, I. T.; Tranitz, H. P.; Wegscheider, W.; Kouwenhoven, L. P.; Vandersypen, L. M. K. *Science* **2005**, *309*, 1346−1350.

(3) Johnson, A. C.; Petta, J. R.; Taylor, J. M.; Yacoby, A.; Lukin, M. D.; Marcus, C. M.; Hanson, M. P.; Gossard, A. C. *Nature* **2005**, *435*, 925−928.

(4) Petta, J. R.; Johnson, A. C.; Taylor, J. M.; Laird, E. A.; Yacoby, A.; Lukin, M. D.; Marcus, C. M.; Hanson, M. P.; Gossard, A. C. *Science* **2005**, *309*, 2180−2184.

(5) Johnson, A. C.; Petta, J. R.; Marcus, C. M.; Hanson, M. P.; Gossard, A. C. *Phys. Rev. B* **2005**, *72*, 165308.

(6) Barthel, C.; Reilly, D. J.; Marcus, C. M.; Hanson, M. P.; Gossard, A. C. *Phys. Rev. Lett.* **2009**, *103*, 160503.

(7) Weber, B.; Tan, Y. H. M.; Mahapatra, S.; Watson, T. F.; Ryu, H.; Rahman, R.; Hollenberg, L. C. L.; Klimeck, G.; Simmons, M. Y. *Nat. Nano* **2014**, *9*, 430−435.

(8) Nguyen, K. T.; Lilly, M. P.; Nielsen, E.; Bishop, N.; Rahman, R.; Young, R.; Wendt, J.; Dominguez, J.; Pluym, T.; Stevens, J.; Lu, T.-M.; Muller, R.; Carroll, M. S. *Nano Lett.* **2013**, *13*, 5785−5790.

(9) Yamahata, G.; Kodera, T.; Churchill, H. O. H.; Uchida, K.; Marcus, C. M.; Oda, S. *Phys. Rev. B* **2012**, *86*, 115322.

(10) Lai, N. S.; Lim, W. H.; Yang, C. H.; Zwanenburg, F. A.; Coish, W. A.; Qassemi, F.; Morello, A.; Dzurak, A. S. *Sci. Rep.* **2011**, *1*, 110.

(11) Liu, H. W.; Fujisawa, T.; Ono, Y.; Inokawa, H.; Fujiwara, A.; Takashina, K.; Hirayama, Y. *Phys. Rev. B* **2008**, *77*, 073310.

(12) Maune, B. M.; Borselli, M. G.; Huang, B.; Ladd, T. D.; Deelman, P. W.; Holabird, K. S.; Kiselev, A. A.; Alvarado-Rodriguez, I.; Ross, R. S.; Schmitz, A. E.; Sokolich, M.; Watson, C. A.; Gyure, M. F.; Hunter, A. T. *Nature* **2012**, *481*, 344−347.

(13) Wu, X.; Ward, D. R.; Prance, J. R.; Kim, D.; Gamble, J. K.; Mohr, R. T.; Shi, Z.; Savage, D. E.; Lagally, M. G.; Friesen, M.; Coppersmith, S. N.; Eriksson, M. A. *Proc. Natl. Acad. Sci. U.S.A.* **2014**, *111*, 11938−11942.

(14) Prance, J. R.; Shi, Z.; Simmons, C. B.; Savage, D. E.; Lagally, M. G.; Schreiber, L. R.; Vandersypen, L. M. K.; Friesen, M.; Joynt, R.; Coppersmith, S. N.; Eriksson, M. A. *Phys. Rev. Lett.* **2012**, *108*, 046808.

(15) Veldhorst, M.; Hwang, J. C. C.; Yang, C. H.; Leenstra, A. W.; de Ronde, B.; Dehollain, J. P.; Muhonen, J. T.; Hudson, F.; Itoh, K. M.; Morello, A.; Dzurak, A. S. *Nat. Nano.* **2014**, *9*, 981−985.

(16) Petersson, K. D.; Smith, C. G.; Anderson, D.; Atkinson, P.; Jones, G. A. C.; Ritchie, D. A. *Nano Lett.* **2010**, *10*, 2789−2793.

(17) Schroer, M. D.; Jung, M.; Petersson, K. D.; Petta, J. R. *Phys. Rev. Lett.* **2012**, *109*, 166804.

(18) Petersson, K. D.; McFaul, L. W.; Schroer, M. D.; Jung, M.; Taylor, J. M.; Houck, A. A.; Petta, J. R. *Nature* **2012**, *490*, 380−383.

(19) Voisin, B.; Nguyen, V.-H.; Renard, J.; Jehl, X.; Barraud, S.; Triozon, F.; Vinet, M.; Duchemin, I.; Niquet, Y.-M.; de Franceschi, S.; Sanquer, M. *Nano Lett.* **2014**, *14*, 2094−2098.

(20) Dupont-Ferrier, E.; Roche, B.; Voisin, B.; Jehl, X.; Wacquez, R.; Vinet, M.; Sanquer, M.; de Franceschi, S. *Phys. Rev. Lett.* **2013**, *110*, 136802.

(21) Gonzalez-Zalba, M. F.; Barraud, S.; Ferguson, A. J.; Betz, A. C. *Nat. Commun.* **2015**, *6*, 6084.

(22) Angus, S. J.; Ferguson, A. J.; Dzurak, A. S.; Clark, R. G. *Nano Lett.* **2007**, *7*, 2051−2055.

(23) Hofheinz, M.; Jehl, X.; Sanquer, M.; Molas, G.; Vinet, M.; Deleonibus, S. *Appl. Phys. Lett.* **2006**, *89*, 143504.

(24) Roche, B.; Voisin, B.; Jehl, X.; Wacquez, R.; Sanquer, M.; Vinet, M.; Deshpande, V.; Previtali, B. *Appl. Phys. Lett.* **2012**, *100*, 032107.

(25) Colless, J. I.; Mahoney, A. C.; Hornibrook, J. M.; Doherty, A. C.; Lu, H.; Gossard, A. C.; Reilly, D. J. *Phys. Rev. Lett.* **2013**, *110*, 046805.

(26) Ciccarelli, C.; Ferguson, A. J. *New J. Phys.* **2011**, *13*, 093015.

(27) Chorley, S. J.; Wabnig, J.; Penfold-Fitch, Z. V.; Petersson, K. D.; Frake, J.; Smith, C. G.; Buitelaar, M. R. *Phys. Rev. Lett.* **2012**, *108*, 036802.

(28) Sellier, H.; Lansbergen, G. P.; Caro, J.; Rogge, S.; Collaert, N.; Ferain, I.; Jurczak, M.; Biesemans, S. *Appl. Phys. Lett.* **2007**, *90*, 073502.

(29) van der Wiel, W. G.; de Franceschi, S.; Elzerman, J. M.; Fujisawa, T.; Tarucha, S.; Kouwenhoven, L. P. *Rev. Mod. Phys.* **2002**, *75*, 1−22.

(30) Sillanpää, M. A.; Lehtinen, T.; Paila, A.; Makhlin, Y.; Roschier, L.; Hakonen, P. J. *Phys. Rev. Lett.* **2005**, *95*, 206806.

(31) Duty, T.; Johansson, G.; Bladh, K.; Gunnarsson, D.; Wilson, C.; Delsing, P. *Phys. Rev. Lett.* **2005**, *95*, 206807.

(32) Cottet, A.; Mora, C.; Kontos, T. *Phys. Rev. B* **2011**, *83*, 121311.

(33) Stepanenko, D.; Rudner, M.; Halperin, B. I.; Loss, D. *Phys. Rev. B* **2012**, *85*, 075416.

(34) Lim, W. H.; et al. *Nanotechnology* **2011**, *22*, 335704.

(35) Saraiva, A. L.; Koiller, B.; Friesen, M. *Phys. Rev. B* **2010**, *82*, 245314.

(36) Culcer, D.; Cywiński, L.; Li, Q.; Hu, X.; Das Sarma, S. *Phys. Rev. B* **2010**, *82*, 155312.

(37) Saraiva, A. L.; Calderón, M. J.; Capaz, R. B.; Hu, X.; Das Sarma, S.; Koiller, B. *Phys. Rev. B* **2011**, *84*, 155320.

(38) Jiang, L.; Yang, C. H.; Pan, Z.; Rossi, A.; Dzurak, A. S.; Culcer, D. *Phys. Rev. B* **2013**, *88*, 085311.

(39) Borselli, M. G.; Ross, R. S.; Kiselev, A. A.; Croke, E. T.; Holabird, K. S.; Deelman, P. W.; Warren, L. D.; Alvarado-Rodriguez, I.; Milosavljevic, I.; Ku, F. C.; Wong, W. S.; Schmitz, A. E.; Sokolich, M.; Gyure, M. F.; Hunter, A. T. *Appl. Phys. Lett.* **2011**, *98*, 123118.